MATERIALS SCIENCE

Sculpted grain boundaries in soft crystals

Xiao Li[1,2]*, José A. Martínez-González[3]*, Orlando Guzmán[4], Xuedan Ma[5], Kangho Park[1], Chun Zhou[1], Yu Kambe[1], Hyeong Min Jin[1], James A. Dolan[1,6], Paul F. Nealey[1,6]†, Juan J. de Pablo[1,6]†

Engineering the grain boundaries of crystalline materials represents an enduring challenge, particularly in the case of soft materials. Grain boundaries, however, can provide preferential sites for chemical reactions, adsorption processes, nucleation of phase transitions, and mechanical transformations. In this work, "soft heteroepitaxy" is used to exert precise control over the lattice orientation of three-dimensional liquid crystalline soft crystals, thereby granting the ability to sculpt the grain boundaries between them. Since these soft crystals are liquid-like in nature, the heteroepitaxy approach introduced here provides a clear strategy to accurately mold liquid-liquid interfaces in structured liquids with a hitherto unavailable level of precision.

INTRODUCTION

Solid-solid grain boundaries—two-dimensional (2D) defects at the intersection of regions of a polycrystalline material having different orientations—are of fundamental importance in determining the bulk physical properties of crystalline solids, including ductility, strength, conductivity, and optical response (*1*–*3*). Hence, they have generated intense scientific and engineering interest throughout the past century (*4*). Grain boundary engineering refers to the systematic manipulation of the presence and morphology of solid-solid grain boundaries, the goal of which is to produce energetically preferential crystalline interfaces whereby atoms from neighboring lattices coincide and achieve a "good atomic fit" (*5*). This is usually accomplished through bulk processing techniques, e.g., thermomechanical treatments, magnetic annealing, plastic deformation, or the application of electric fields (*4*). Surface techniques, e.g., the modulation of substrate topography or crystalline orientation, may be applied to obtain grain boundaries with desired locations and specified misfit angles but only for 2D systems such as graphene (*6*, *7*). However, whether by bulk or surface techniques, precise and direct control of grain boundary position, length, and morphology in crystalline solids remains a grand challenge.

Liquid-liquid interfaces, on the other hand, arise at the intersection of immiscible—and, by definition, amorphous—liquids and are of considerable interest in a wide range of contexts, including membrane self-assembly, nanoparticle self-assembly, ion transfer, and localized chemical reactions (*8*–*11*). Furthermore, liquid-liquid interfaces are particularly attractive due to their capacity to induce self-assembly and the ease with which they reach a stable state (*12*). However, liquid-liquid interfaces are governed by interfacial tension and are therefore limited to a few select geometries (e.g., spheres, planes, and menisci) that minimize interfacial area.

Liquid crystalline "soft crystals" exhibit a hybrid set of properties that are traditionally associated with both crystalline solids and amorphous liquids; in particular, molecules can flow while maintaining a 3D crystalline order on the mesoscale. Grain boundaries between regions of a polycrystalline soft crystal with different orientations are therefore compliant, thereby making soft crystals amenable to a new class of soft matter grain boundary engineering techniques. In addition, liquid crystalline soft crystals may serve as useful mesoscale and soft matter analog of atomic crystals (*13*), whereby the liquid-like nature and larger length scales allow grain boundary phenomena that are difficult to access in analogous atomic crystals.

Among liquid crystals, the so-called blue phases (BPs) are of particular interest as they share the properties of both a 3D cubic crystal and a liquid. Different strategies have been developed to produce BP monodomains, and these studies reveal that control of the BP lattice orientation and formation of dislocation-free macroscopic BP crystals are both particularly difficult to achieve (*14*–*18*). In this respect, the work by Zheng *et al.* (*18*) represented an outstanding advance with respect to the control of the optical response of BPs, and they demonstrated a means of using light to produce rewriteable, on-demand patterns of BP monodomains. In a previous work, we developed a strategy to design and fabricate chemical patterns that enable the formation of single crystals of BP with on-demand lattice orientations (*19*, *20*). A common feature in both these works—and other similar methods—is the roughness of the boundaries of the BP domains that are formed. That is, consistent and variable BP patterns or shapes can be achieved, but roughness at the edges of these patterns/shapes is revealed when zooming in on the borders at micron and/or submicron scales. In addition, by successfully fabricating BP single crystals, we have been able to analyze soft crystal nucleation and growth on chemically patterned substrates at substantial larger length scales than of atomic crystals. This allowed the observation that the BPII-BPI phase transformation assisted by a chemically patterned surface is martensitic in nature, is therefore directly analogous to classic diffusionless phase transformations found in solid crystals (*13*), and enriches the understanding of soft crystal crystallization and growth. To further explore BP liquid crystals as mesoscale and soft matter analogs of atomic crystals in the context of grain boundaries, in this work, a "soft heteroepitaxy" strategy, based on the accurate design and implementation of lithographically patterned chemical surfaces, is introduced to manipulate the orientation of BPs. Using this strategy, the grain boundaries between adjacent single crystalline domains are stabilized and sculpted with extreme precision, down to length scales that commensurate with the lattice spacing of the crystal. Given the liquid nature of the BPs,

[1]Pritzker School of Molecular Engineering, The University of Chicago, Chicago, IL 60637, USA. [2]Department of Materials Science and Engineering, University of North Texas, Denton, TX 76203, USA. [3]Facultad de Ciencias, Universidad Autónoma de San Luis Potosí, Av. Parque Chapultepec 1570, San Luis Potosí 78295, SLP, México. [4]Departamento de Física, Universidad Autonóma Metropolitana, Av. San Rafael Atlixco 186, Ciudad de México 09340, México. [5]Center for Nanoscale Materials, Argonne National Laboratory, Lemont, IL 60439, USA. [6]Center for Molecular Engineering, Argonne National Laboratory, Lemont, IL 60439, USA.
*These authors contributed equally to this work.
†Corresponding author. Email: nealey@uchicago.edu (P.F.N.); depablo@uchicago.edu (J.J.d.P.)

it becomes possible to localize and shape grain boundaries. We further demonstrate how to control and manipulate the optical properties of precisely shaped ideal soft crystals through the application of an external stimulus, i.e., temperature or an electric field, and discuss how this may be used to create diffractive photonic devices with improved performance. We therefore show that it is possible to fully overcome, on one hand, the hitherto limited grain morphologies accessible with liquid-liquid interfaces and, on the other, challenges that are traditionally associated with manipulation of solid crystalline materials.

RESULTS

Heteroepitaxy growth of BP single crystals on chemically patterned surfaces

BP liquid crystals are chiral materials in which molecules orient and organize into double-twist cylinders (DTCs) (*21*, *22*). Depending on the thermodynamic conditions, DTCs can arrange into a 3D, crystalline body–centered cubic structure, the so-called BPI, or into a simple cubic structure referred to as the BPII. The DTC array is interspersed by a well-defined network of liquid crystalline line defects, the lattice parameters of which are on the submicron scale for both BPI and BPII. Recent work has shown that, in the absence of grain boundaries, the crystal-crystal transition from BPI to the BPII can be extremely fast and can be understood as the liquid analog of a classic martensitic transformation (*13*). Because of the length scale of the lattice parameters, BPs exhibit Bragg reflections for visible light. This photonic crystal property, as well as fast electro-optical switching with submillisecond response times, makes BPs particularly attractive for photonic applications, biosensing, and display technologies (*23*–*27*).

For the chiral liquid crystal considered in our experiments, the BPs can be obtained either upon heating or cooling with the following phase transition temperatures: $T_{\text{Chol-BPI}} = 39.9° \pm 0.05°C$, $T_{\text{BPI-BPII}} = 40.7° \pm 0.05°C$, and $T_{\text{BPII-Iso}} = 42.9° \pm 0.05°C$, where Chol denotes the cholesteric phase and Iso denotes the isotropic phase (*13*, *19*). For BPII, the unit cell size is $a_{\text{BPII}} = 150$ nm, and light is reflected by the (100), (110), and (111) planes at the peak wavelengths $\lambda_{(100)} = 450$ nm (visible), $\lambda_{(110)} = 320$ nm (ultraviolet), and $\lambda_{(111)} = 260$ nm (ultraviolet), respectively. Figure 1A shows a representation of the BPI and BPII DTC arrays and disclination lines for different lattice orientations. We denote $\text{BPII}_{(hkl)}$ as a BPII crystal where the (*hkl*) lattice plane is parallel to the underlying substrate; $\text{BPI}_{(hkl)}$ denotes the same for a BPI crystal. To achieve $\text{BPII}_{(100)}$ soft crystals, we rely on a "stripe pattern" (SP) consisting of an alternating array of regions of planar (silicon substrate) and homeotropic (polymer brush) liquid crystal anchoring, where each region has a width equal to $a_{\text{BPII}}/2 = 75$ nm. To instead create a $\text{BPII}_{(110)}$ soft crystal, the lithographic pattern consists of a hexagonal array of rectangular homeotropic regions against a planar anchoring background ["rectangular pattern" (RP)]; for $\text{BPII}_{(111)}$ soft crystals, we use circular regions ["circular pattern" (CP)] (detailed pattern characteristics are provided in fig. S1). The geometry and dimensions of the chemical patterns corresponding to each of the different lattice orientations of BPII are based on continuum simulations, as reported in our previous work (*19*). Briefly, BPII with specific out-of-plane orientations were simulated and subjected to uniform homeotropic anchoring conditions on both surfaces. After the system relaxed to its equilibrium state, we obtained the order parameter map at the interface for each lattice condition. Information regarding the preferred molecular alignment was extracted from this order parameter map and simplified into a binary pattern consisting of regions of planar and homeotropic anchoring. Therefore, a specific pattern was obtained, which was capable of stabilizing each lattice orientation. Through theoretical mean field calculations of the free energy, we determined and used the optimal dimensions of the planar and homeotropic regions for the chemical pattern preparation. The chiral liquid crystal material is confined within a hybrid cell that consists of an octadecyltrichlorosiline-coated glass top surface (homeotropic anchoring) and a chemically patterned silicon substrate (homeotropic and planar anchoring) as the bottom surface (Fig. 1B), and the cell thickness is kept as 3.5 μm in all samples (*28*).

Sculpting grain boundary of BP with specific lattice orientations

We rely on heteroepitaxy to grow not single-crystal solids but single-crystal liquid crystalline BPs by controlling the nucleation and growth of their cubic lattices with specific orientations (*19*). To illustrate this, we fabricate a binary-anchoring (i.e., planar-homeotropic) patterned substrate where the pattern-pattern border follows a characteristic C shape. The inner and outer regions of the C shape favor the formation of BPs oriented to reflect light from two different crystallographic planes (Fig. 1C). In the BPII temperature regime, $\text{BPII}_{(100)}$ and $\text{BPII}_{(110)}$ distortion-free soft crystals are formed inside and outside the C region, respectively (Fig. 1D); in contrast, in the BPI temperature range, $\text{BPI}_{(110)}$ and $\text{BPI}_{(200)}$ monodomains are formed (Fig. 1D). In both cases, the BP liquid-liquid grain boundaries are 2D surfaces whose basis follows, with nanoscale precision, the path traced by the pattern-pattern borders printed on the substrate, particularly in the BPII temperature regime. This is despite the fact that the C shape has several curved regions that were deliberately created along its border and, therefore, regions of complicated and substantial curvature between adjacent areas with different crystalline orientations (Fig. 1C). We also tested the response of the sample to an in-plane electric field (Fig. 1E). The system is brought to the BPI regime ($T = 39.8°C$), where it presents $\text{BPI}_{(110)}$ and $\text{BPI}_{(200)}$ domains. When a 3.5-V voltage is applied, a phase transformation to $\text{BPII}_{(100)}$ (within the inner region) and $\text{BPII}_{(110)}$ (in the outer region) is induced. By removing the applied voltage, the system returns to the initial BPI state, demonstrating that BP martensitic transformations can be reversibly controlled by applying an electric field.

Soft crystal epitaxial growth to maintain grain boundary

To understand the mechanism of soft crystal growth for two adjacent domains with different orientations, we first examine how BPs form above patterns of different symmetries and areas, and how these BP domains compete at a BPII-BPII interface. To this end, we consider three combinations of patterns: an SP region adjacent to an RP region (SP-RP; Fig. 2A), an SP region adjacent to a homeotropic region (SP-H; Fig. 2B), and an SP region adjacent to a CP region (SP-CP; Fig. 2C). In all cases, we patterned a total region of 440 μm by 440 μm with alternating stripe-like sections of an SP-RP, SP-H, or SP-CP array. The length and width of the patterned sections are kept at 440 and 10 μm, respectively. Thus, in Fig. 2, the nomenclature "stripe 10–rectangular 10" refers to an SP region with a width of 10 μm adjacent to an RP region with a width of 10 μm.

We begin by examining the nucleation, growth, and formation of BPII from the isotropic state upon cooling. The initial temperature

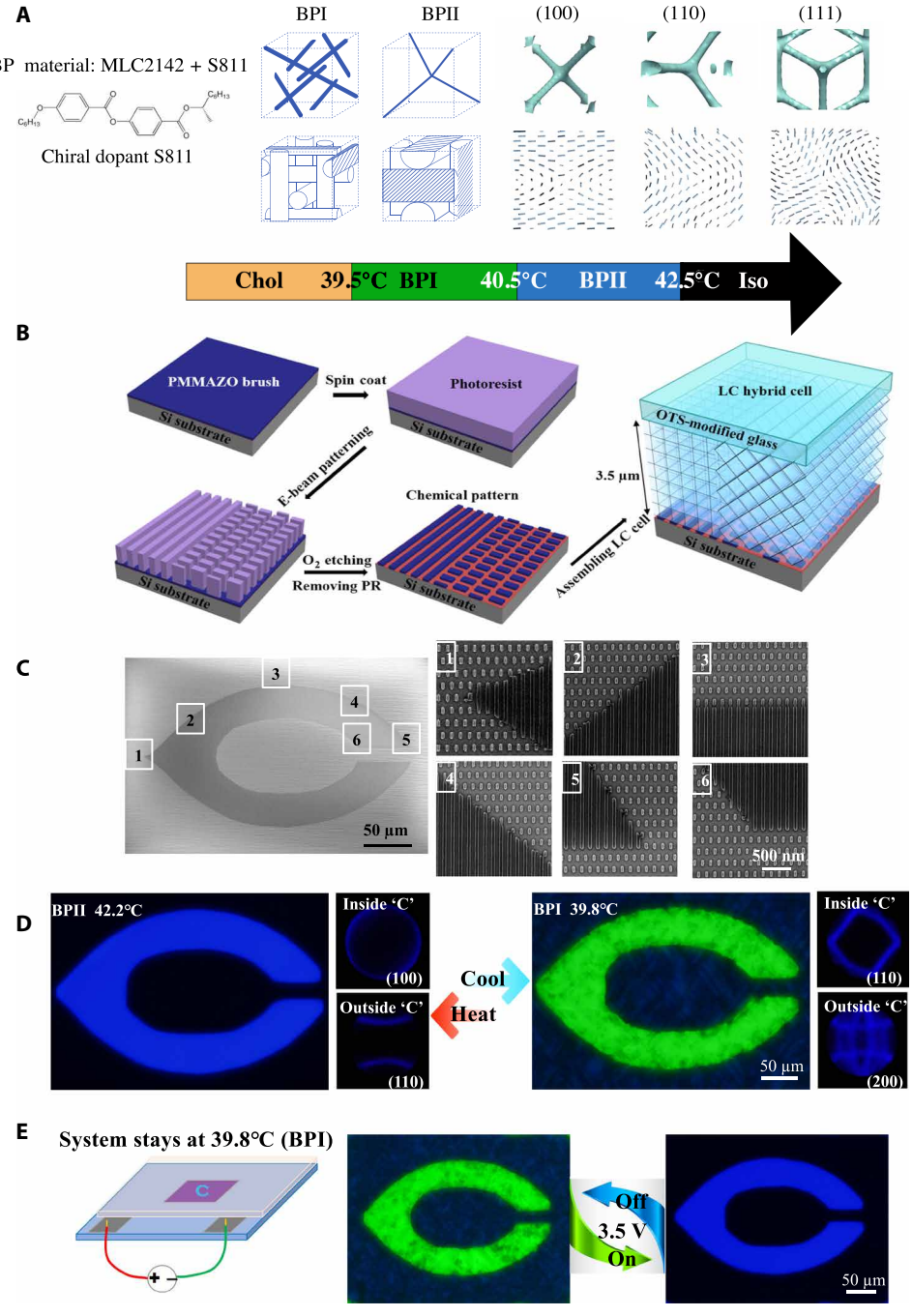

Fig. 1. Engineered C-shaped soft crystal surrounded by a differently oriented soft crystal. (**A**) Nematic liquid crystal (LC) host (MLC2142) and chiral dopant (S811) for BP material; unit cell structures and disclination lines for BPI and BPII; disclination line structure of BPII viewed along three lattice planes (top) and their corresponding director fields (bottom). (**B**) Fabrication scheme for soft heteroepitaxy chemical patterns on a silicon substrate. BP material confined between octadecyltrichlorosiline (OTS)–coated top glass (homeotropic anchoring) and chemically patterned substrate (alternating homeotropic and planar anchoring) with a gap of 3.5 μm. (**C**) A SP surface designed as a "C" surrounded by a RP background. Left: Scanning electron microscopy (SEM) image marked with six different areas. Right: Detailed pattern information. (**D**) Reflection optical microscopy images with Kossel diagrams corresponding to $BPII_{(100)}$—or $BPI_{(110)}$—inside the "C" region and $BPII_{(110)}$—or $BPI_{(200)}$—outside. (**E**) Reflection optical microscopy images showing the optical response of the material at 39.8°C (i.e., within the BPI temperature range) when a voltage of 3.5 V is applied.

of the isotropic phase was 42.9°C, and the liquid crystal is then taken to the BPII temperature region following a one-step quench process, which results in the formation of $BPII_{(100)}$, $BPII_{(110)}$, and $BPII_{(111)}$ soft crystals atop the SP, RP, and CP regions, respectively. Optical microscopy images of the SP-RP array are shown in Fig. 2A, which demonstrate that the SP-RP stripe array stabilizes alternating $BPII_{(100)}$ and $BPII_{(110)}$ regions with sharp interfaces between them, even after a prolonged period of time (10 min). Recall that only the $BPII_{(100)}$

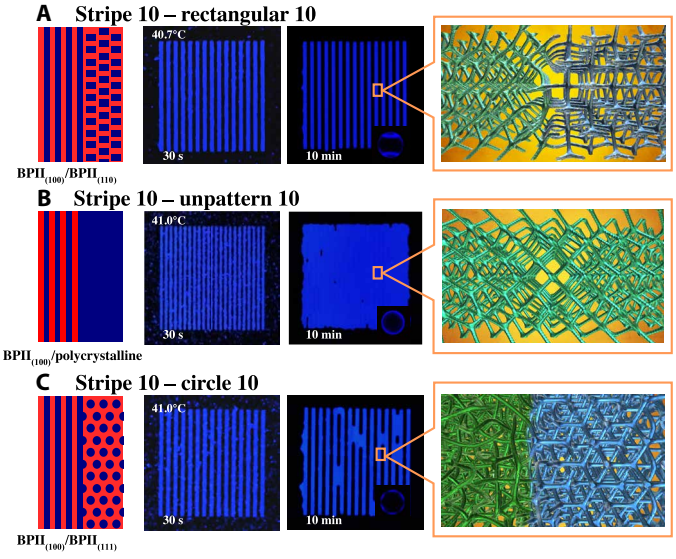

Fig. 2. Grain boundaries at pattern boundaries. SP adjacent to (**A**) RP regions, (**B**) homeotropic (unpatterned), and (**C**) CP regions. Reflection optical microscopy images of the corresponding patterned areas are also shown, along with simulation results of the disclination lines for the $BPII_{(100)}$-$BPII_{(110)}$ and $BPII_{(100)}$-$BPII_{(111)}$ interfaces, respectively.

domains reflect visible (blue) light and that the out-of-plane orientation of all the BPII regions can be identified by their characteristic Kossel diagrams. It is possible to achieve well-defined and stable $BPII_{(100)}$-$BPII_{(110)}$ interfaces. Only those interfaces at the array's furthest edges appear rough with irregular shape and only then because these correspond to interfaces between the patterned substrate and the unpatterned, uncontrolled homeotropic background. BPs that grow over unpatterned homeotropic regions show a polycrystalline texture, dominated mainly by $BPII_{(111)}$ platelets of different in-plane orientations. Both the SP-H (Fig. 2B) and SP-CP (Fig. 2C) arrays differ notably from the SP-RP array: The interfaces are neither sharp nor stabilized. This is particularly apparent for the SP-H array, where $BPII_{(100)}$ soft crystals eventually dominate the entire area. Since BPs are liquid in nature, all the grain boundaries are liquid-liquid interfaces. Therefore, for the $BPII_{(100)}$-$BPII_{(110)}$ case, these liquid-liquid interfaces are found above the pattern-pattern boundaries. Using continuum mean field calculations, we simulate $BPII_{(100)}$-$BPII_{(110)}$, $BPII_{(100)}$-H, and $BPII_{(100)}$-$BPII_{(111)}$ coexisting systems (Fig. 2, A to C, right) and find that only the $BPII_{(100)}$-$BPII_{(110)}$ interface is predicted to be stable. For this case, we estimate the corresponding interfacial free energy to be $f^{S}_{100-110} \approx 5 \times 10^{-6}\ \mathrm{Jm}^{-2}$ (fig. S2 and the Supplementary Materials). Similar results can be obtained upon heating from the cholesteric phase; i.e., an alternating array of $BPII_{(100)}$-$BPII_{(110)}$ or $BPII_{(111)}$-$BPII_{(110)}$ soft crystals can be obtained when using SP-RP or SP-CP areas, showing sharp or rough interfaces, respectively (fig. S3).

To determine the lateral dimensions that a patterned region must have to grow and support a stable BPII domain, square SP regions of different areas can be embedded within a homeotropic background (fig. S4A). As shown in fig. S4A, 10 μm by 10 μm (or larger)–patterned domains lead to $BPII_{(100)}$ soft crystals that remain unaffected by neighboring regions. They can even propagate slightly into external, unpatterned regions. Having demonstrated, both experimentally and through simulations, that $BPII_{(100)}$-$BPII_{(110)}$ interfaces follow SP-RP boundaries, we now consider a different SP-RP combination that consists of a 137 μm by 200 μm rectangular SP region surrounded by a 300 μm by 380 μm RP area. We further embed this hybrid patterned region within an unpatterned and uniform homeotropic region (Fig. 3A). Heat is then applied, starting from the cholesteric phase. In the cholesteric regime, the SP area shows a variety of green-blue colors, while the contrast between the RP area and the outer homeotropic region is not obvious (Fig. 3B at 27.0°C). Upon increasing the temperature to the BPI regime, the patterned areas do not selectively stabilize specific lattice planes (Fig. 3B at 40.5° and 41.1°C); the whole surface is covered with a green and dark blue platelet mixture consisting of $BPI_{(110)}$ and $BPI_{(200)}$ grains (recall that SP and RP patterns were specifically designed to nucleate BPII, rather than BPI, lattice orientations). Once the temperature reaches the BPII regime, a single $BPII_{(100)}$ soft crystal forms above the SP region with its characteristic blue color, while for the RP region, a single $BPII_{(110)}$ soft crystal is obtained (this region appears dark because the wavelength of the reflected light is $\lambda_{(110)} = 320$ nm, i.e., in the ultraviolet). The outer homeotropic background region exhibits a polycrystalline texture that is primarily dominated by $BPII_{(111)}$ platelets and some $BPII_{(100)}$ and $BPII_{(110)}$ grains that disappear at ≈41.8°C. In all cases, the Kossel diagrams confirm the symmetry of the soft crystals (Fig. 3C). This binary SP-RP–patterned substrate represents the first example of an engineered rectangular soft crystal grain, where the grain boundary is a sharp liquid-liquid interface separating two crystalline regions. Furthermore, the lateral resolution of the boundaries between two patterns has been explored with a similar pattern design as fig. S4A but with the unpatterned neighboring regions being replaced by the RP as shown in fig. S4B. When the lateral dimensions of the chemical pattern that promotes the nucleation and growth of a $BPII_{(100)}$ single crystal is below 20 μm, the forming $BPII_{(100)}$ onto this pattern can be affected by the neighboring $BPII_{(110)}$ due to their similar densities of free energy (*19*); however, the border that divides two differently patterned areas coincides with nanoscale precision, with the grain boundary of the BP crystals, which form atop their corresponding patterns. Hence, although the patterned regions must be minimally large to support the BPII domains, the grain boundary between these regions may be placed and controlled with nanoscale precision.

Binary pattern array as a stimuli responsive optical platform

We conclude this work with an assembly that serves to illustrate possible optical applications of this proposed liquid-liquid grain boundary engineering approach. A periodic 2D diffraction array is built from square SP regions, each region measuring 60 μm by 60 μm with an additional 60 μm of separation between them. We embed such an array within either a homeotropic or RP background to produce array 1 (Fig. 4A) and array 2 (Fig. 4B), respectively. In both cases, we apply heat to observe successive Chol→BPI→BPII phase transitions (fig. S5). Once the system reaches a stable BPII, cooling is applied to return the sample to the cholesteric phase. The reflected diffraction patterns of the arrays at different temperatures and times are obtained by impinging a 445-nm laser perpendicularly to the samples (Fig. 4C). The results for array 1 are presented in Fig. 4D, which shows those multiple, clearly defined maxima in the diffraction pattern that are produced when $BPII_{(100)}$ single crystals cover the SP regions. The results for array 1 along the phase sequence Chol→BPI→BPII are as follows (fig. S5A). The initial cholesteric phase does not present a defined diffraction pattern due to the poor light reflection at 445 nm

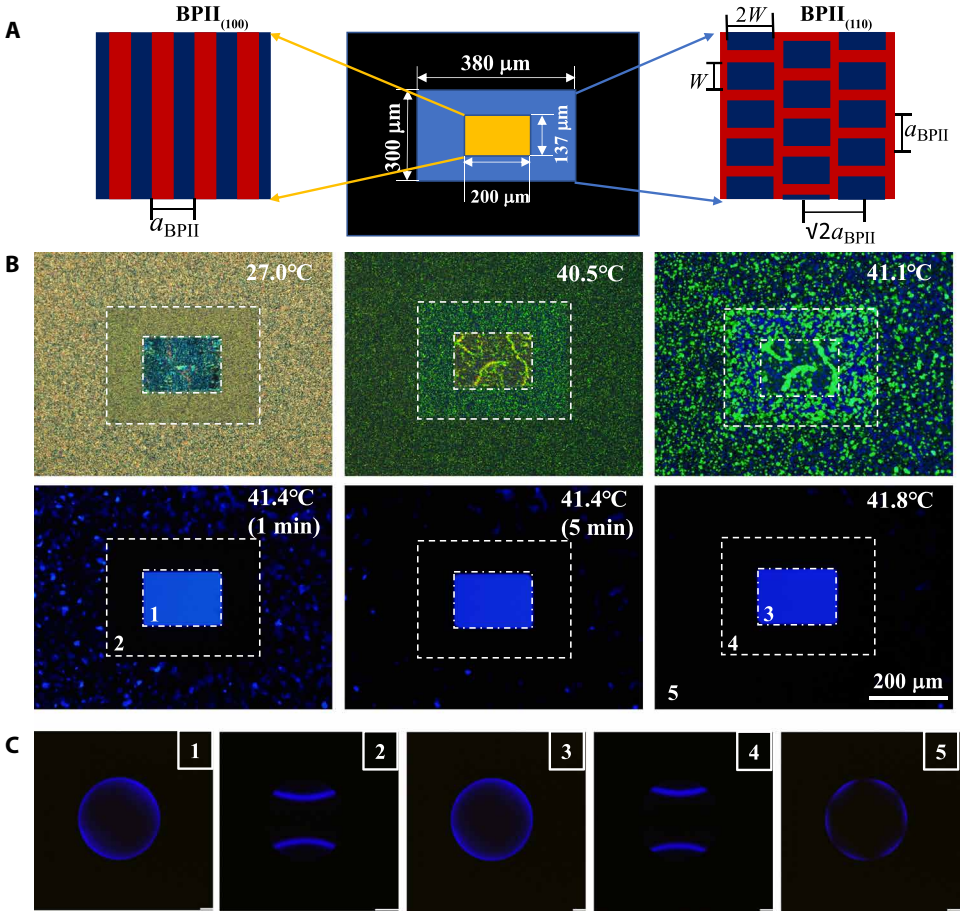

Fig. 3. Engineered rectangular grains. (**A**) Chemically patterned surface designed as an SP area surrounded by an RP region. Red regions correspond to homeotropic anchoring, and blue regions correspond to planar anchoring. (**B**) Reflection optical microscopy images of the system at different temperatures during heating. (**C**) Kossel diagrams indicating the BPII symmetry corresponding to different pattern regions marked in (B).

and the weak contrast between the patterned and unpatterned regions. In the BPI regime, we observe a polycrystalline texture consisting of a mixture of $BPI_{(110)}$ (green) and $BPI_{(200)}$ (blue) grains; as expected, the square SP regions favor $BPI_{(110)}$ nucleation (*19*). Since the reflection peak of $BPI_{(110)}$ corresponds to a wavelength of 550 nm, diffraction patterns cannot be obtained with the 445-nm laser. However, once the temperature reaches the BPII regime, $BPII_{(100)}$ soft crystals spontaneously nucleate and grow on the square SP areas; the reflection peak of the $BPII_{(100)}$ soft crystals (450 nm) now matches the laser wavelength. The noise in the corresponding diffraction pattern is due to the nonuniformity of the single-crystal $BPII_{(100)}$ regions (e.g., their poorly defined boundaries) and the polycrystalline nature of the $BPII_{(111)}$ background. Last, upon cooling, the diffraction pattern disappears, and in the BPI temperature regime, a polycrystalline $BPI_{(110)}$ monodomain covers the entire array 1 region. Once again, in the cholesteric phase, the SP regions show a nonuniform blue color with a corresponding diffuse diffraction pattern.

The noise in the diffraction pattern produced by array 1, caused by the homeotropic background, is always present because uniform homeotropic anchoring does not result in any particular BP lattice orientation. For this reason, we designed array 2 (Fig. 4E) to ensure that the background (RP) selects exclusively for $BPII_{(110)}$. On heating, the initial cholesteric state does not present a defined diffraction pattern (fig. S5B). However, at the BPII regime, the square SP regions lead to square-shaped grains of $BPII_{(100)}$, while the RP background induces the formation of a single $BPII_{(110)}$ soft crystal. Now, in contrast to array 1, all the BPII grain boundaries are clearly delineated by the pattern-pattern boundaries. At this point, the system can be taken back to the BPI regime by cooling. Unlike array 1, the system now visibly renders the transformation from well-defined BPII soft crystals, which only differ in their lattice orientation, to BPI soft crystals: Fig. 4E shows that $BPII_{(100)}$ soft crystals transform into $BPI_{(110)}$ over the square SP regions, while $BPII_{(110)}$ single crystals transform into $BPI_{(200)}$ over the RP background. Similar to the BPII regime, at the BPI temperature range, array 2 still shows sufficiently well-defined boundaries between BPI grains. Last, once again in the cholesteric state, two different textures can be identified within the square SP regions and the RP background as a result of the $BPI_{(110)}$-Chol and $BPI_{(200)}$-Chol phase transitions.

DISCUSSION

The results presented above demonstrate that substrates patterned at the nanoscale are able to induce BP soft crystal formation with predetermined lattice orientation in a manner that is faster and more reproducible than by conventional methods (e.g., slow cooling). We

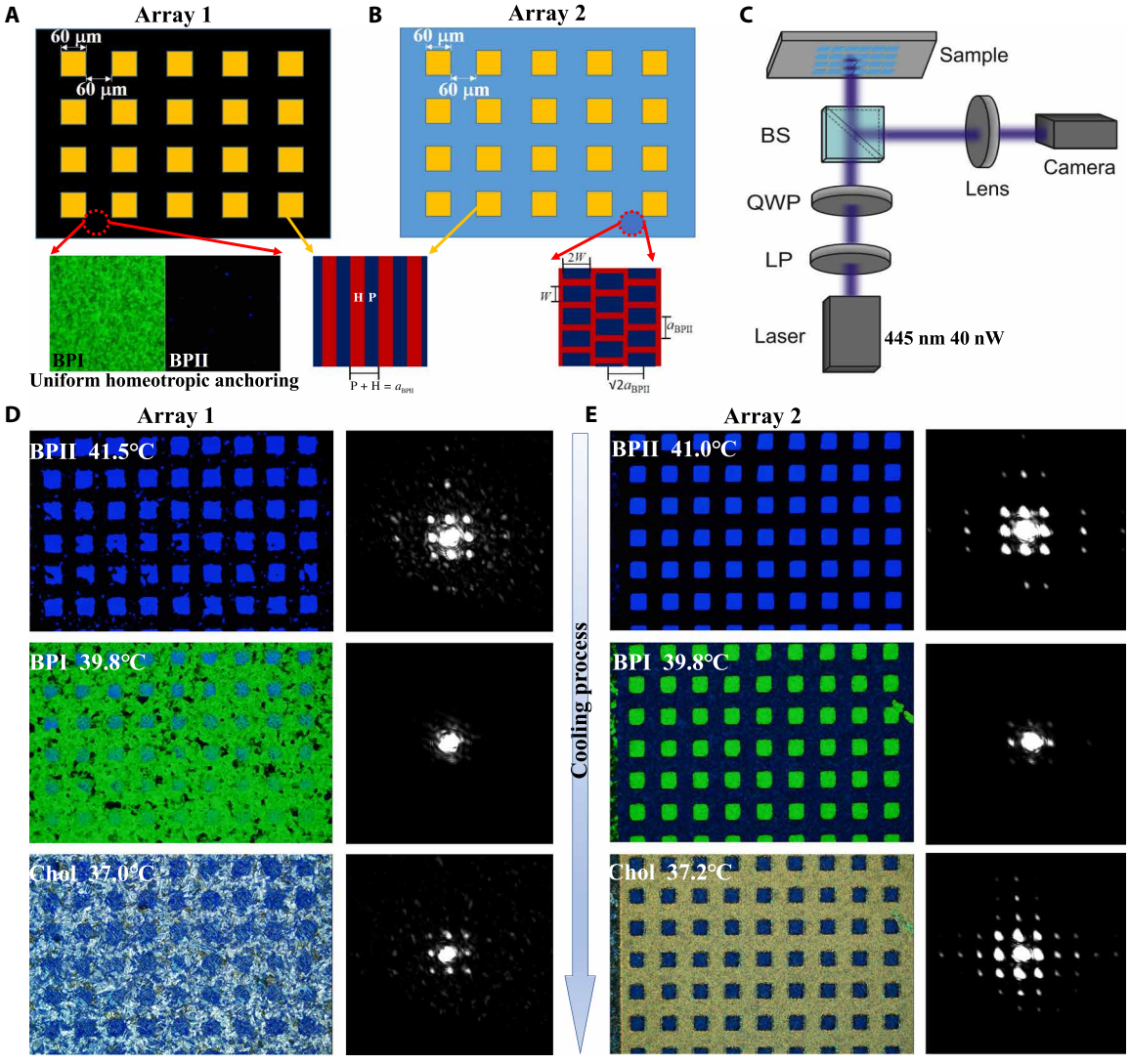

Fig. 4. Binary pattern array as a stimuli responsive platform. (**A**) Chemically patterned surface designed as 60 μm by 60 μm SP area within a uniform homeotropic anchoring background. Reflection optical microscopy images of BPI and BPII on the uniform homeotropic anchoring surface. (**B**) Chemically patterned surface designed as an SP area surrounded by an RP background. (**C**) Optical setup for diffraction detection. A 445-nm laser light is converted to circularly polarized light after successively passing through a linear polarizer (LP) and a quarter waveplate (QWP). The circularly polarized light impinges on the sample by passing through a beam splitter (BS), generating the diffraction pattern. The diffractive light was projected on a black screen. (**D** and **E**) Reflection optical microscopy images of system array 1 (D) and array 2 (E), with their corresponding diffraction patterns at different temperatures during the cooling process.

refer to this strategy as soft heteroepitaxy due to its analogy to solid-state heteroepitaxy, in which one crystalline material is deposited atop another. Using appropriately patterned substrates, it is possible to produce single-crystal BP soft crystals with a variety of in- and out-of-plane orientations. Control over the grain boundaries is achieved using a substrate with two different pattern symmetries. These sculpted grain boundaries are also liquid-liquid interfaces. Our results indicate that the substrate patterns, originally developed to selectively nucleate specific BPII orientations, predetermine the lattice orientation of the BPI monodomain crystal obtained by cooling its BPII antecessor: A $BPII_{(100)}$ single crystal grown over a SP transforms into a $BPI_{(110)}$, while an initial BPII(110) grain will transform into a $BPI_{(200)}$.

Figure S6 (A and B) shows enlarged images of the SP and RP samples and the corresponding reflection spectra, which serve to better visualize the transformations shown in Figs. 1 and 4 upon cooling. From fig. S6, it can be seen that during the $BPII_{(100)}$-$BPI_{(110)}$ and $BPII_{(110)}$-$BPI_{(200)}$ transformations, the system exhibits a crosshatched texture, which is associated with martensitic phase transformations. In solid (i.e., atomic) crystals, a martensitic transformation is a diffusionless crystal-crystal transformation where the atoms move in a coordinated and cooperative manner. Here, BP soft crystal structures are composed of arrays of supramolecular DTCs. The BPI-BPII transformations are produced by the coordinated and cooperative motion of the liquid crystal molecules without diffusion of the DTCs—the liquid analog of a classic martensitic transformation (*13*). With respect to the behavior of the diffractive array shown in Fig. 4A, our results represent a notable improvement over those reported by Zheng *et al.* (*18*); instead of an array of uniform BP regions in a

background of randomly oriented BP grains, here, we introduce an array of aligned BPII in a background of aligned BPII, where both the in- and out-of-plane orientations of the two regions can be manipulated. Our platform allows us to stabilize and control the optical behavior in the BPII, BPI, and cholesteric phase regimes, thereby leading to a remarkable improvement in 2D diffraction grating response, as can be seen in Fig. 4E and fig. S7. The 2D diffraction patterns are visible in a temperature range (38.2° to 37.2°C) due to the contrast in reflectivity of the liquid crystal phases within this temperature range and at the wavelength of interest (fig. S5B). The simulated diffraction patterns for both cases in fig. S7 (A and B) illustrate how the sharp crystalline grain boundary suppresses the second-order peaks. Whether the second-order peaks are present is a function of both the structure factor—the Fourier transform of the square array (identical in both cases)—and the form factor—the Fourier transform of the "pixel" (which has either sharp or rough boundaries). The form factor in the case of sharp grain boundaries exhibits minima, which coincide with the second-order peaks, hence suppressing those peaks. The sharpness of the grain boundary is therefore directly related to the diffraction properties of the grating. In addition, within the cholesteric temperature regime, the uniform blue color arises from the well-aligned cholesteric phase (assisted by the nano-SP with a pitch corresponding to the wavelength of blue light) instead of the crystal structure of a BP (Kossel diagram in fig. S6).

To the best of our knowledge, there is no precedent in the literature for the creation of precisely sculpted crystal grain boundaries in either solid- or liquid-state research. The results shown in Figs. 1 and 4 become remarkable when one considers that BP unit cells are composed of billions of molecules, 2D patterns are used to exert control over these 3D liquid materials, and the precise manner in which different lattices and defects meet at their boundaries. More generally, given the wide range of phenomena that occur at liquid-liquid interfaces, the use of BPs to produce sculpted boundaries offers promise both for the development of new technologies and for the fundamental study of a variety of interfacial processes. The ability to combine different BP regions of arbitrary shape, free of grains, and distortions, offers distinct opportunities for design and production of dynamically transformable and stimuli-responsive 3D soft crystals.

MATERIALS AND METHODS

The detailed information of materials and sample preparations can be found in (*13*) and (*29*).

Characterization

The PMMAZO brush thickness was determined by a Woollam VUV-VASE32 variable angle spectroscopic ellipsometer. Optical characterization was performed using cross-polarized and reflection mode with an Olympus BX60 microscope with 10×/50× objectives, Bertrand lens, and 405-nm monochromic light filter. Samples were heated up to the isotropic phase using a Linkam PE120 temperature controller controlling the hot stage at different rates. Chemical patterns were observed by scanning electron microscopy (SEM; ZEISS MERLIN). BP type and crystal orientation were detected by Kossel diagrams (*19*, *30*). A spectrophotometer (USB4000, Ocean Optics) was used to measure ultraviolet-visible spectra of different BP films. The laser source with output wavelength of 445 nm/40 nW was used to detect the diffraction of the binary pattern array. A laser light with 445-nm wavelength was converted to circular polarized light after successively passing through a linear polarizer and a quarter wave plate. The circularly polarized light impinges on the sample by passing through beam splitters, generating the diffraction pattern. The diffractive light was projected on a black screen.

Heating process and cooling process

The sample was settled on a precisely controlled hot stage (PE120, Linkam). The heating process consists of step increments of the temperature of the samples at a rate of 0.2°C/min, usually starting from the cholesteric phase (25°C) to reaching the isotropic phase at 42.9°C. For cooling, we used a one-step quench process. The temperature was reduced from the isotropic temperature of 42.9° to ~40.9°C (i.e., 0.2°C above $T_{BPI\text{-}BPII}$), where the desired BPII primarily nucleates and grows over the chemical pattern area and stays at certain temperature for different times.

Application of electric field

The external electric field (Gamry 600 Ref Potentiostat/Galvanostat) was applied between two electrodes on conductive Si substrate with a constant voltage at 3.5 V, switching between on and off.

SUPPLEMENTARY MATERIALS

Supplementary material for this article is available at http://advances.sciencemag.org/cgi/content/full/5/11/eaax9112/DC1

REFERENCES AND NOTES

1. V. Randle, Grain boundary engineering: An overview after 25 years. *Mater. Sci. Technol.* **26**, 253–261 (2010).
2. G. Palumbo, E. M. Lehockey, P. Lin, Applications for grain boundary engineered materials. *JOM* **50**, 40–43 (1998).
3. Y. Gao, Y. Zhang, B. W. Beeler, Y. Wang, Self-organized multigrain with special grain boundaries produced by phase transformation cycling. *Phys. Rev. Mater.* **2**, 073402 (2018).
4. T. Watanabe, Grain boundary engineering: Historical perspective and future prospects. *J. Mater. Sci.* **46**, 4095–4115 (2011).
5. N. Shibata, F. Oba, T. Yamanoto, Y. Ikuhara, Structure, energy and solute segregation behaviour of [110] symmetric tilt grain boundaries in yttria-stabilized cubic zirconia. *Philos. Mag.* **84**, 2381–2415 (2004).
6. Y. Wang, V. H. Crespi, Theory of finite-length grain boundaries of controlled misfit angle in two-dimensional materials. *Nano Lett.* **17**, 5297–5303 (2017).
7. J. Lahiri, Y. Lin, P. Bozkurt, I. I. Oleynik, M. Batzill, An extended defect in graphene as a metallic wire. *Nat. Nanotechnol.* **5**, 326–329 (2010).
8. A. Mendoza-Meinhardt, L. Botto, A. Mata, A fluidic device for the controlled formation and real-time monitoring of soft membranes self-assembled at liquid interfaces. *Sci. Rep.* **8**, 2900 (2018).
9. W. H. Binder, Supramolecular assembly of nanoparticles at liquid–liquid interfaces. *Angew. Chem. Int. Ed.* **44**, 5172–5175 (2005).
10. Z. Liang, W. Bu, K. J. Schweighofer, D. J. Walwark Jr., J. S. Harvey, G. R. Hanlon, D. Amoanu, C. Erol, I. Benjamin, M. L. Schlossman, Nanoscale view of assisted ion transport across the liquid-liquid interface. *Proc. Natl. Acad. Sci. U.S.A.* **116**, 18227–18232 (2019).
11. P. Peljo, M. Bichon, H. H. Girault, Ion transfer battery: Storing energy by transferring ions across liquid–liquid interfaces. *Chem. Commun.* **52**, 9761–9764 (2016).
12. J. J. Armao IV, I. Nyrkova, G. Fuks, A. Osypenko, M. Maaloum, E. Moulin, A. Arenal, O. Gavat, A. Semenov, N. Giuseppone, Anisotropic self-assembly of supramolecular

polymers and plasmonic nanoparticles at the liquid–liquid interface. *J. Am. Chem. Soc.* **139**, 2345–2350 (2017).
13. X. Li, J. A. Martínez-González, J. P. Hernandez-Ortiz, A. Ramírez-Hernández, Y. Zhou, M. Sadati, R. Zhang, P. F. Nealey, J. J. de Pablo, Mesoscale martensitic transformation in single crystals of topological defects. *Proc. Natl. Acad. Sci. U.S.A.* **114**, 10011–10016 (2017).
14. P. Nayek, H. Jeong, H. R. Park, S.-W. Kang, S. H. Lee, H. S. Park, H. J. Lee, H. S. Kim, Tailoring monodomain in blue phase liquid crystal by surface pinning effect. *Appl. Phys. Express* **5**, 051701 (2012).
15. J. Yan, S.-T. Wu, K.-L. Cheng, J.-W. Shiu, A full-color reflective display using polymer-stabilized blue phase liquid crystal. *Appl. Phys. Lett.* **102**, 081102 (2013).
16. H. Claus, O. Willekens, O. Chojnowska, R. Dąbrowski, J. Beeckman, K. Neyts, Inducing monodomain blue phase liquid crystals by long-lasting voltage application during temperature variation. *Liq. Cryst.* **43**, 688–693 (2016).
17. E. Oton, E. Netter, T. Nakano, Y. D. Katayama, F. Inoue, Monodomain blue phase liquid crystal layers for phase modulation. *Sci. Rep.* **7**, 44575 (2017).
18. Z.-G. Zheng, C.-L. Yuan, W. Hu, H. K. Bisoyi, M.-J. Tang, Z. Liu, P.-Z. Sun, W.-Q. Yang, X.-Q. Wang, D. Shen, Y. Li, F. Ye, Y.-Q. Lu, G. Li, Q. Li, Light patterned crystallographic direction of a self-organized 3D soft photonic crystal. *Adv. Mater.* **29**, 1703165 (2017).
19. J. A. Martínez-González, X. Li, M. Sadati, Y. Zhou, R. Zhang, P. F. Nealey, J. J. de Pablo, Directed self-assembly of liquid-crystalline blue-phases into ideal single crystals. *Nat. Commun.* **8**, 15854 (2017).
20. X. Li, J. A. Martínez-González, K. Park, C. Yu, Y. Zhou, J. J. de Pablo, P. F. Nealey, Perfection in nucleation and growth of blue-phase single crystals: Small free-energy required to self-assemble at specific lattice orientation. *ACS Appl. Mater. Interfaces* **11**, 9487–9495 (2019).
21. D. C. Wright, N. D. Mermin, Crystalline liquids: The blue phases. *Rev. Mod. Phys.* **61**, 385–432 (1989).
22. P. P. Crooker, The cholesteric blue phase: A progress report. *Mol. Liq. Cryst.* **98**, 31–45 (1983).
23. S. S. Gandhi, M. S. Kim, J.-Y. Hwang, L.-C. Chien, Electro-optical memory of a nanoengineered amorphous blue-phase III polymer scaffold. *Adv. Mater.* **28**, 8998–9005 (2016).
24. F. Castles, F. V. Day, S. M. Morris, D.-H. Ko, D. J. Gardiner, M. M. Qasim, S. Nosheen, P. J. W. Hands, S. S. Choi, R. H. Friend, H. J. Coles, Blue-phase templated fabrication of three-dimensional nanostructures for photonic applications. *Nat. Mater.* **11**, 599–603 (2012).
25. S. Yokoyama, S. Mashiko, H. Kikuchi, K. Uchida, T. Nagamura, Laser emission from a polymer-stabilized liquid-crystalline blue phase. *Adv. Mater.* **18**, 48–51 (2006).
26. J. A. Martínez-González, Y. Zhou, M. Rahimi, E. Bukusoglu, N. L. Abbott, J. J. de Pablo, Blue-phase liquid crystal droplets. *Proc. Natl. Acad. Sci. U.S.A.* **112**, 13195–13200 (2015).
27. Y. Huang, H. Chen, G. Tan, H. Tobata, S.-i. Yamanoto, E. Okabe, Y.-F. Lan, C.-Y. Tsai, S.-T. Wu, Optimized blue-phase liquid crystal for fieldsequential-color displays. *Opt. Mater. Express* **7**, 641–650 (2017).
28. X. Li, J. A. Martinez-Gonzalez, J. J. de Pablo, P. F. Nealey, Thickness dependence of forming single crystal by liquid-crystalline blue phase on chemically patterned surface, in *Emerging Liquid Crystal Technologies* XIII (International Society for Optics and Photonics, 2018), p. 1055514.
29. X. Li, J. C. Armas-Perez, J. A. Martinez-Gonzalez, X. Liu, H. Xie, C. Bishop, J. P. Hernandez-Ortiz, R. Zhang, J. J. de Pablo, P. F. Nealey, Directed self-assembly of nematic liquid crystals on chemically patterned surfaces: Morphological states and transitions. *Soft Matter* **12**, 8595–8605 (2016).
30. R. Miller, H. Gleeson, Order parameter measurements from the Kossel diagrams of the liquid-crystal blue phases. *Phys. Rev. E* **52**, 5011–5016 (1995).
31. M. Ravnik, S. Žumer, Landau–de Gennes modelling of nematic liquid crystal colloids. *Liq. Cryst.* **36**, 1201–1214 (2009).
32. J.-B. Fournier, P. Galatola, Modeling planar degenerate wetting and anchoring in nematic liquid crystals. *Europhys. Lett.* **72**, 403–409 (2005).
33. G. P. Alexander, J. M. Yeomans, Numerical results for the blue phases. *Liq. Cryst.* **36**, 1215–1227 (2009).

Acknowledgments
Funding: This work was supported by the U.S. Department of Energy, Office of Science, Basic Energy Sciences, Materials Sciences and Engineering Division. We acknowledge the use of the facility resources for the experimental part from the Center for Nanoscale Materials, a U.S. Department of Energy (DOE) Office of Science User Facility operated for the DOE Office of Science by Argonne National Laboratory under contract no. DE-AC02-06CH11357 (e-beam patterning and optical microscope); The University of Chicago MRSEC Shared User Facilities (NSF DMR-1420709) (SEM characterization); and the use of the Pritzker Nanofabrication Facility of the PME at the University of Chicago (NSF ECCS-1542205) (e-beam patterning and RIE).
Author contributions: X.L. and J.A.M.-G. contributed equally to this work. X.L. and P.F.N. conceived and performed experiments. J.A.M.-G., O.G., and J.J.d.P. conceived and performed numerical simulations and theoretical calculations. X.L., J.A.M.-G., O.G., J.A.D., J.J.d.P., and P.F.N. wrote the manuscript. J.J.d.P. and P.F.N. guided the work. Other authors contribute to: optical setup for diffraction detection: X.M.; electric field setup: Y.K.; Optical diffraction pattern simulation: H.M.J.; E-beam patterning: C.Z.; Optical observation during thermal process: K.P.
Competing interests: The authors declare that they have no competing interests. **Data and materials availability:** All data needed to evaluate the conclusions in the paper are present in the paper and/or the Supplementary Materials. Additional data related to this paper may be requested from the authors.

Submitted 3 May 2019
Accepted 7 October 2019
Published 29 November 2019
10.1126/sciadv.aax9112

Citation: X. Li, J. A. Martínez-González, O. Guzmán, X. Ma, K. Park, C. Zhou, Y. Kambe, H. M. Jin, J. A. Dolan, P. F. Nealey, J. J. de Pablo, Sculpted grain boundaries in soft crystals. *Sci. Adv.* **5**, eaax9112 (2019).